

1 **Understanding the Utility of Endocardial Electrocardiographic Imaging in Epi-**
2 **Endocardial Mapping of 3D Reentrant Circuits**

3 Wang: ECGi of 3D Reentrant Circuit

4 Maryam Toloubidokhti^a, Omar A Gharbia^b, Adityo Parkosa^c, Natalia Trayanova^c, Alexios
5 Hadjis^d, Roderick Tung^e, Saman Nazarian^f, John L. Sapp^g, Linwei Wang^a

6

7 ^aCollege of Computing and Information Sciences, Rochester Institute of Technology,
8 Rochester, NY, USA

9 ^bDepartment of Otolaryngology, School of Medicine, University of Utah, Salt Lake City, UT,
10 USA

11 ^cDepartment of Biomedical Engineering, Johns Hopkins University, Baltimore, MD, USA

12 ^dHôpital du Sacré-Cœur de Montréal, Montreal, Quebec, Canada

13 ^eCollege of Medicine, University of Arizona, AZ, USA

14 ^fSchool of Medicine, University of Pennsylvania, Philadelphia, USA

15 ^gDepartment of Medicine, QEII Health Sciences Centre, Halifax, NS, Canada

16

17 **Abstract**

18 **Background:** Studies of VT mechanisms are largely based on a 2D portrait of reentrant
19 circuits on one surface of the heart. This oversimplifies the 3D circuit that involves the depth
20 of the myocardium. Simultaneous epicardial and endocardial (epi-endo) mapping was shown
21 to facilitate a 3D delineation of VT circuits, which is however difficult via invasive mapping.

22

23 **Objective:** This study investigates the capability of noninvasive epicardial-endocardial
24 electrocardiographic imaging (ECGI) to elucidate the 3D construct of VT circuits,

25 emphasizing the differentiation of epicardial, endocardial, and intramural circuits and to
26 determine the proximity of mid-wall exits to the epicardial or endocardial surfaces.

27

28 **Methods:** 120-lead ECGs of VT in combination with subject-specific heart-torso geometry
29 are used to compute unipolar electrograms (CEGM) on ventricular epicardium and
30 endocardia. Activation isochrones are constructed, and the percentage of activation within
31 VT cycle length is calculated on each surface. This classifies VT circuits into 2D (surface
32 only), uniform transmural, nonuniform transmural, and mid-myocardial (focal on surfaces).
33 Furthermore, the endocardial breakthrough time was accurately measured using Laplacian
34 eigenmaps, and by correlating the delay time of the epi-endo breakthroughs, the relative
35 distance of a mid-wall exit to the epicardium or the endocardium surfaces was identified.

36

37 **Results:** We analyzed 23 simulated and in-vivo VT circuits on post-infarction porcine hearts.
38 In simulated circuits, ECGI classified 21% as 2D and 78% as 3D: 82.6% of these were
39 correctly classified. The relative timing between epicardial and endocardial breakthroughs
40 was correctly captured across all cases. In in-vivo circuits, ECGI classified 25% as 2D and 75%
41 as 3D: in all cases, circuit exits and entrances were consistent with potential critical isthmus
42 delineated from combined LGE-MRI and catheter mapping data.

43

44 **Conclusions:** ECGI epi-endo mapping has the potential for fast delineation of 3D VT
45 circuits, which may augment detailed catheter mapping for VT ablation.

46

47 **Keywords:** 3D Ventricular tachycardia, Electrocardiographic imaging, Endocardial
48 Breakthrough

49

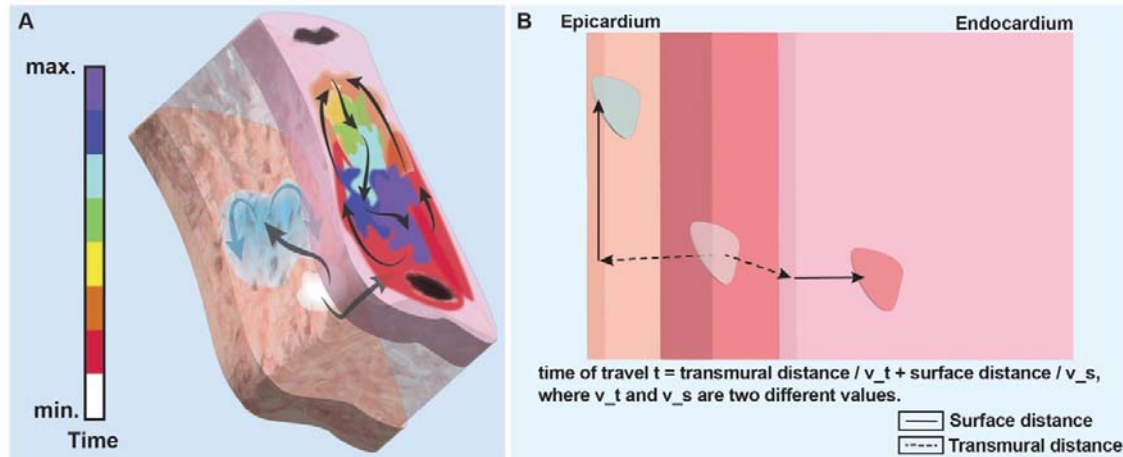


Figure 1: Illustration of a 3D reentrant circuit and its epicardial and endocardial observations. A: A mid-wall exit exhibits as a partial rotation at one surface and a focal activation at the other surface. B. Illustration of a simplified relation between the breakthrough times on both surfaces and the exit site.

50 **Introduction**

51 Most life-threatening ventricular tachycardia (VT) episodes involve reentrant circuits
52 facilitated by narrow strands of surviving tissue in areas of patchy scar or at scar borders
53 (1,2). Current analyses of the morphology of reentrant circuits primarily rely on catheter
54 mapping on one surface of the ventricles (epicardium or endocardium). This provides a two-
55 dimensional (2D) simplified view and interpretation of the morphology of the reentrant
56 circuit, assuming all of its critical components to be on one surface.
57 The spatiotemporal construct of a reentrant circuit, however, is naturally 3D involving mid-
58 myocardium wall. As illustrated in Fig. 1, the electrical current may exit from the protected
59 central isthmus anywhere in the thickness of the myocardial wall. After traveling across the
60 wall, it then breakthroughs to both surfaces of the wall. While observing the earliest site of
61 activation on the surface where measurement is taken (*e.g.*, via catheter mapping), it is
62 important to note that – depending on the 3D construct of the reentrant circuit – the observed
63 surface breakthrough sites may or may not be near the actual exit sites both in transmural

64 depth and surface distances. In an inspiring recent study by Tung et al (3), simultaneous
65 epicardial and endocardial (epi-endo) catheter mapping was used to show that the information
66 on the two surfaces can be combined to facilitate *qualitative* inferences about mid-myocardial
67 activation of 3D reentrant circuits (3). Such knowledge can be important for informing
68 ablation strategies, but unfortunately is mostly missing in the current clinical practice due to
69 the difficulty to obtain simultaneous high-resolution epi-endo catheter mapping, especially
70 for VT episodes where up to 90% of the circuits are too short-lived to permit detailed
71 mapping (2,4).

72

73 Noninvasive electrocardiographic imaging (ECGI) – a family of computational approaches to
74 reconstructing the temporal course of cardiac electrical sources from body-surface
75 electrocardiograms (ECGs) and patient-specific heart-torso geometry – offers a natural
76 candidate to fill this critical gap. However, two critical questions remain. First, despite its
77 widely-explored use for a variety of cardiac arrhythmias such as atrial fibrillation (5) and
78 premature ventricular contraction (6), ECGI techniques have been mainly accepted for their
79 epicardial imaging abilities: the clinical feasibility and utility of endocardial ECGI solutions
80 remain less established despite numerous technical studies (14,15). Second, the study of
81 ECGI in ventricular reentrant circuits have been mostly limited to epicardial solutions
82 including both torso-tank (7,8) and human studies (9–12): notably, a recent study has shown
83 that epicardial ECGI is able to localize the origin of VT circuits with sufficient accuracy to
84 support targeted mapping for ablation (13). Only a small number of studies have investigated
85 the potential of simultaneous epi-endocardial ECGI (14,15) in mapping reentrant VT,
86 although remaining at qualitative inspections of the activation pattern or localization of the
87 site of earliest activation on one of the ventricular surfaces. It has not been yet investigated

88 whether or how epicardial-endocardial ECGI solutions may be combined to elucidate the 3D
89 construct of VT reentrant circuits.

90

91 In this study, we will provide answers to these two open questions by examining the
92 feasibility of inferring the 3D construct of a reentrant circuit from what ECGI can reconstruct
93 on both the epicardial and endocardial surfaces of the wall after breakthroughs. The
94 contribution of this study is two-fold. First, with a deep dive into ECGI-reconstructed
95 unipolar electrograms at the endocardium, we show that – while the spatiotemporal amplitude
96 of the reconstructed signals shows significant discrepancies from the ground truth, the phase
97 of the signal in the VT cycle is accurately preserved. We further show that by leveraging
98 Laplacian eigenmaps to quantify the progression of endocardial activation in a two-
99 dimensional space, we were able to identify the timing of endocardial breakthrough from
100 endocardial ECGI solutions. These findings present one of the first steps towards discovering
101 clinically relevant information hidden within endocardial ECGI solutions, going beyond
102 signal amplitudes. Second, we take a step further built on the results presented in (3) to
103 perform a mechanistic study to use ECGI to infer the *unobserved* mid-wall components of a
104 3D circuit from the *observed* activity after breakthroughs at the two surfaces of the wall.
105 Following (3), we first show that the gross epicardial and endocardial activation patterns,
106 based on the percentage of circuit activation observed on each surface, can be combined to
107 categorize the reentrant circuit into 2D, 3D, and mid-myocardial constructs.

108

109 Due to the fundamental challenges to obtain either clinical (or even experimntal data) for the
110 transmural morphology of a reentrant circuit, we carry out our investigations in two types of
111 data with different levels of reference data available. First, we leverage 23 previously-
112 published high-fidelity simulations of 3D reentrant circuits virtually induced on post-

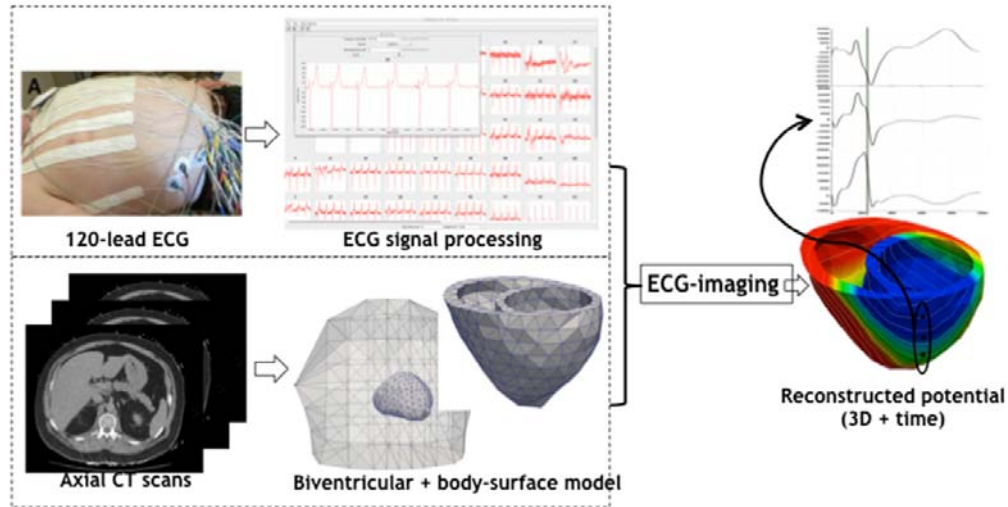
113 infarction porcine model (16), to support a mechanistic study where detailed 3D morphology
114 of the reentrant circuits is available. We then extend the investigations to four *in-vivo* animal
115 models where – although 3D mapping data of the reentrant circuit is not available – potential
116 critical isthmus for the reentrant circuits and its transmural depth are estimated from
117 combined analysis of contrast-enhanced magnetic resonance imaging (CE-MRI) and
118 electroanatomic mapping (EAM) data.

119

120 Experimental results from the *in-silico* mechanistic study showed that activations observed
121 on the two surfaces – especially the timing and distance of the breakthrough sites – were well
122 correlated with the 3D locations of the exit sites of the reentrant circuits. On these data,
123 combining epicardial and endocardial ECGI activation patterns were able to correctly
124 characterize the categories of 3D reentrant circuits in 83% of the cases, and combining ECGI
125 epi-endocardial breakthrough timing was able to successfully differentiate sub-endocardial
126 versus sub-epicardial exit sites in 100% of the cases. In *in-vivo* animal models, the epicardial
127 and endocardial breakthrough time as discovered by ECGI was also able to correctly differentiate
128 the one sub-epicardial, one sub-endocardial, and two mid-wall circuits as suggested by the
129 combined MRI-EAM analysis, with the locations of these breakthroughs qualitatively
130 corroborated by MRI and EAM data.

131

132 These results provided evidence that ECGI may be a viable tool for providing noninvasive
133 information at the epicardial and endocardial surfaces – especially in the form of the timing
134 and location of the breakthrough sites at these surfaces – that can be combined to infer the 3D
135 construct of a reentrant circuit. This may have a potential to inform ablation strategies, such as
136 epicardial versus endocardial access or the appropriate penetration depth necessary for an
137 ablation lesion, prior to the procedural.



138

139 **Methods**

140 *Epi-Endo Electrocardiographic Imaging*

141 We consider ECGI for reconstructing the time sequence of extracellular potential (*i.e.*,
142 unipolar electrograms) throughout the epicardial and endocardial surfaces (15). By
143 representing the bi-ventricular model with a closed surface as illustrated in Fig. 2, the
144 relationship between the heart-surface electrogram and body-surface ECG is governed by a
145 Laplace's equation defined by the quasi-static electromagnetism (17). When solved
146 numerically on discrete surface bi-ventricular and torso meshes, we obtain a forward matrix
147 \mathbf{H} using open-source SCIRun toolkit (19) that relates unipolar potential at the
148 ventricular surface to body-surface potential though at any time

Figure2: ECGI workflow. Reconstruction of heart electrical potentials from body surface potentials by obtaining body surface recordings from 120 leads placed on the subject's body and generating heart and torso meshes from MRI images.

149 instant. Given a time sequence of $\phi_b(t)$, we solve $\phi_v(t)$ c independently at each time instant
150 by solving the second-order Tikhonov regularization (18)

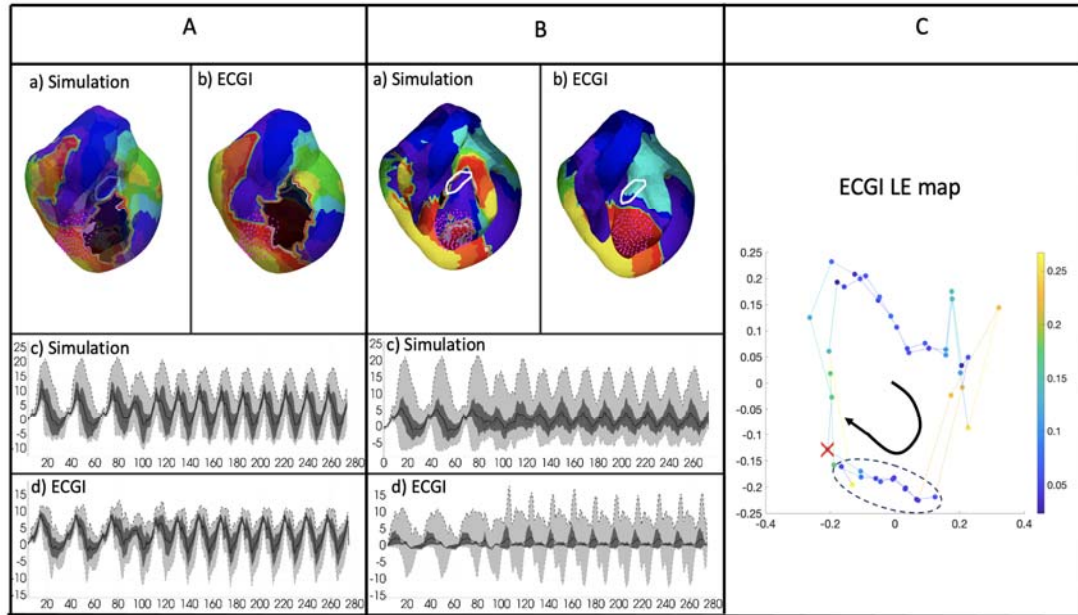
$$\widehat{\phi}_v(t) = \underset{\phi_v}{\operatorname{argmin}} \left\{ \|\phi_b(t) - \mathbf{H}\phi_v(t)\|_2^2 + \lambda \|\mathbf{L}\phi_v(t)\|_2^2 \right\}, t = 1, 2, \dots, T$$

151 where the first term minimizes the error of fitting body-surface ECG data, and the second
152 term regularizes the solution. Here, the regularization matrix \mathbf{L} is chosen to be the surface
153 Laplacian operator and the regularization parameter λ is tuned empirically. The inverse
154 calculation was done using a custom Matlab routine.

155

156 ***3D Categorization of Reentrant Circuits***

157 Following (3), we simultaneously quantify the activation isochrones on both the epicardial
158 and endocardial surfaces, and use their relation to categorize the observed reentrant circuit.
159 To extract activation isochronal maps, we first apply the Hilbert transform to heart-surface
160 EGMs to obtain the instantaneous phase signal at each spatial location as described in (20).
161 The activation wave-front at any time instant is then determined as the location with phase =
162 $\pi/2$ as suggested by (15,21). From the isochronal maps, we locate the region where rotations
163 of activation can be seen and identify the portion of rotation – out of the full cycle of VT –
164 that is visible on each surface. The activation gap, as defined in (3), is the period of time
165 when activation of the rotation is missing from a surface. If a rotation is not at least partially
166 visible on a surface, the activation is considered focal on that. Finally, we combine the
167 isochronal maps on both surfaces to categorize the 3D characteristics of a reentrant circuits
168 following the definition used in (3):



- 169 • 2D circuits: A complete rotation without any activation gap (all isochronal colors) is
170 seen on one surface, and focal activation is seen on the other surface.
- 171 • 3D non-uniform circuits: Partial rotations with activation gaps are observed on one or
172 both surfaces.
- 173 • 3D uniform circuits: Complete rotations are observed on both surfaces. This was not
174 observed in the data used in this study.

Figure3: Analyzing the ECGI solutions on epicardium and endocardium. A) Comparing ECGI pattern and amplitude on epicardium B) Comparing ECGI solution pattern and amplitude on endocardium C) example of identifying the endocardial breakthrough time from the Laplacian eigenmap of the ECGI solution.

- 175 • Mid-myocardial circuit: Focal activation is observed on both surfaces.

176

177 *Identifying the Timing and Location of Endocardial Breakthrough Sites*

178 Epicardial ECGI solutions are generally consistent in reconstructing the amplitude of the
179 potential signals in the time domain, as illustrated in Fig. 3A. In comparison, endocardial
180 ECGI solutions tend to create artificial macroscopic rotation patterns that exhibit large
181 discrepancy from the actual potential signal, suggesting significant errors in the
182 reconstruction of the signals in the time domain as illustrated in Fig. 3B. Does this suggest
183 that ECGI solutions are completely invalid on the endocardial surfaces?

184

185 A closer look at the endocardial ECGI solutions reveals that, while the amplitude of the
186 signal $\phi_v(t)$ are incorrectly reconstructed at each time instant t , a notable pattern of slow
187 progression followed by fast progression is consistently observed in each VT cycle in the
188 reconstructed $\phi_v(t)$ sequence on the endocardium. We hypothesize that the phase of this high
189 dimensional signal $\phi_v(t)$ – its progression in the periodic cycle of the VT beats – is captured
190 in ECGI solutions, and that the time instant following the slow progression can be identified
191 as the time of breakthrough on the endocardium.

192

193 To extract the phase of $\phi_v(t)$ for discrete snapshots of the temporal signal at $t = 0, 1, \dots, T$,
194 we leverage Laplacian eigenmaps (LE) (26) as a nonlinear dimensionality reduction method

195 to obtain a low-dimensional representation of the spatial-temporal signal sequence of ECGI
196 solutions on the endocardium. The primary objective of using LE is to explore and uncover
197 potential patterns in the spatiotemporal activation sequences over time by visualizing this
198 activity in a lower dimensional space. The method constructs a graph using pairwise
199 distances between data points and a heatmap kernel, to capture relationships between the
200 values of the neighbor nodes. Subsequently, the graph Laplacian matrix is computed and
201 subjected to Singular Value Decomposition (SVD). Through the SVD, the significance of the
202 manifold's coordinates is determined and ranked, from which we then use directions
203 associated with the two largest eigenvalues to preserve features of the original signals in a
204 significantly reduced space.

205

206 The resulting two-dimensional coordinate space, termed the "LE space", represents a
207 manifold or a trajectory of the endocardial ECGI solution pattern over time where, as
208 illustrated in Fig. 3C, the reconstructed full endocardial potential at time frame t is
209 represented by a unique position on the manifold in the two-dimensional LE space and each
210 "loop" represents the progression of $\phi_v(t)$ within a monomorphic VT cycle. As shown, the
211 duration of slow progression can be characterized with narrowly spaced points whereas the
212 duration of rapid progression can be characterized with sparsely spaced points. We thus use
213 the distance between the 2D points, i.e., $v(k) = ||d(k) - d(k - 1)||^2$, as a surrogate
214 measure of the speed of progression (color coded in Fig 3C), and identify the time of
215 endocardial breakthrough as the time instant at which $\phi_v(t)$ exits from the duration of slow
216 progression, as marked by the red cross in Fig 3C.

217

218 ***From Surface Breakthrough Sites to Exit Sites Beneath the Surface***

219 We further investigate if the breakthrough sites observed on the two surfaces bounding the
220 myocardial wall can be combined to reveal the location of circuit exits inside the wall. Fig.
221 1B illustrates our intuition: that the relative timing and location of the breakthrough sites on
222 the two surfaces of the wall reflects how the electrical current travels to the two surfaces after
223 exiting from the scar. To quantify this, we proceed in two steps.

224

225 As a primary focus, we attempt to correlate the delay time of the two breakthroughs to the
226 relative proximity of the mid-wall exits to either of the two surfaces bounding the wall. We
227 primarily focus on differentiating whether a mid-wall exit is closer to the epicardium or the
228 endocardium, where the latter can be either left endocardium or right endocardium depending
229 on the location of the reentrant circuits. To do so, we record the time difference between the
230 epicardial and endocardial breakthroughs $dt = t_{epi} - t_{endo}$, and study the use of dt for
231 differentiating sub-epicardial/sub-endocardial exit sites. The reference sub-epicardial versus
232 sub-endocardial location of the actual mid-wall exit is determined based on the actual mid-
233 wall location of the exit in simulation data, and by the MRI and/or ablation evidence in
234 animal and human data. We hypothesize that a negative dt , with an earlier breakthrough at
235 the endocardium, indicates a sub-endocardial exit site, a positive dt with an earlier epicardial
236 breakthrough indicates a sub-epicardial exit site, and a dt close to 0 indicate a mid-wall exit
237 site. We confirm this hypothesis by the epicardial-endocardial breakthrough time identified in
238 the simulated reentrant circuits, and then test the ability of epi-endocardial ECGI solutions in
239 capturing this.

240

241 **Materials and Data**

242 *Simulation Reentrant Circuits*

243 The use of simulation data, while associated with limitations pertaining to validity in
244 comparison to real data, provides unique availability of detailed 3D data of the reentrant
245 circuits that is not possible in current experimental or clinical settings. Here, we utilize
246 reentrant circuits virtually induced on detailed ventricular model with high-resolution scar
247 morphology from a previous study (16). As detailed in (16), simulation data were generated
248 on eight chronically infarcted porcine hearts. Detailed models of the intact large animal
249 ventricles were constructed from *in-vivo* MRI images, with image-based fiber orientation and
250 detailed scar geometry obtained at a voxel size of 0.03125 mm^3 . Electrical wave propagation
251 was modeled by the monodomain formulation, and the simulations were performed using the
252 software package CARP (CardioSolv, LLC) on a parallel computing platform (16).
253 Monomorphic VTs were induced in all the hearts using a clinical S1-S2-S3 programmed
254 electrical stimulation protocol (22), applied from 27 pacing sites selected on the basis of a
255 modified American Heart Association segment designation. A total of 23 sustained VTs
256 (lasting for at least 2s after the last pacing stimulus) were induced and used in this study. For
257 each sustained VT, the pathway of the reentrant circuit in the form of a string loop was
258 identified by connecting seed points along the fastest part of the 3D activation of the circuit
259 as described in (16),
260
261 To simulate body-surface ECGs corresponding to each reentrant circuit, each animal heart
262 was placed in a human torso model consisting of a triangular mesh with 120 vertices
263 representing the positions of surface ECG leads. Epi-endocardial extracellular potential was
264 simulated from each reentrant circuit solving the Poisson's equation underlying the quasi-

265 static electromagnetism using a custom software (23). This served as the cardiac source
266 model and used to generate the 120-lead body-surface ECG using the forward operator
267 specific to each heart-torso pair constructed using the SCIRun software (19). The surface ECG
268 was added with 20-dB Gaussian noise and input for ECGI reconstruction of epi-endo EGMs.
269

270 ***Chronic Post-Infarction Animal Models of Reentrant Circuits***

271 Four swine models, weighed 35-45 kg, were used in a study protocol in accordance with the
272 Johns Hopkins University Institutional Animal Care and Use Committee (16,24). Prior to the
273 invasive procedure of MI creation, swine were anesthetized with mechanical ventilation using
274 a combination of tiletamine, zolazepam, ketamine, and xylazine and maintained under
275 sedation using 1-2 % isoflurane. In all animals, MI was created by inserting a guiding
276 catheter into the left coronary artery and occluding the left anterior descending (LAD)
277 coronary artery using an angioplasty balloon for two hours.

278

279 At approximately eight to ten weeks post-MI, DCE-CMR was performed in all swine models
280 using a 3-T scanner (Prisma, Siemens Healthcare) in 20-30 minutes after injection of
281 Gadopentetate dimeglumine (0.20 mmol/kg, Magnevist, Bayer, Leverkusen, Germany). A
282 free-breathing navigator-gated three-dimensional inversion recovery T1w sequence was used
283 with typical imaging parameters as: inversion time = 400 ms, flip angle = 25°, repetition time
284 = 5.4 ms, echo time = 2.7 ms, reconstructed pixel size = 1.1 x 1.1 x 1.1 mm with interpolation
285 in the slice direction, 12 segments per imaging window, GRAPPA acceleration factor (R) = 2,
286 FOV = 300 x 220 mm, matrix = 272 x 200, bandwidth = 200 Hz/Pixel, scan time = 15-20 min.

287

288 Within one week after DCE-CMR, the electrophysiological study was performed using the
289 NavX mapping system (EnSite Velocity, St. Jude Medical). Prior to the electrophysiology

290 study, 18 strips of 120 disposable radiolucent electrodes were placed on the swine torso
291 following the standard Dalhousie mapping protocol (25). Approximately ten surface
292 electrodes were removed to accommodate the placement of NavX pads. The rest of the
293 electrodes remained attached throughout the electrophysiology study to record surface ECG
294 during induced VT.

295

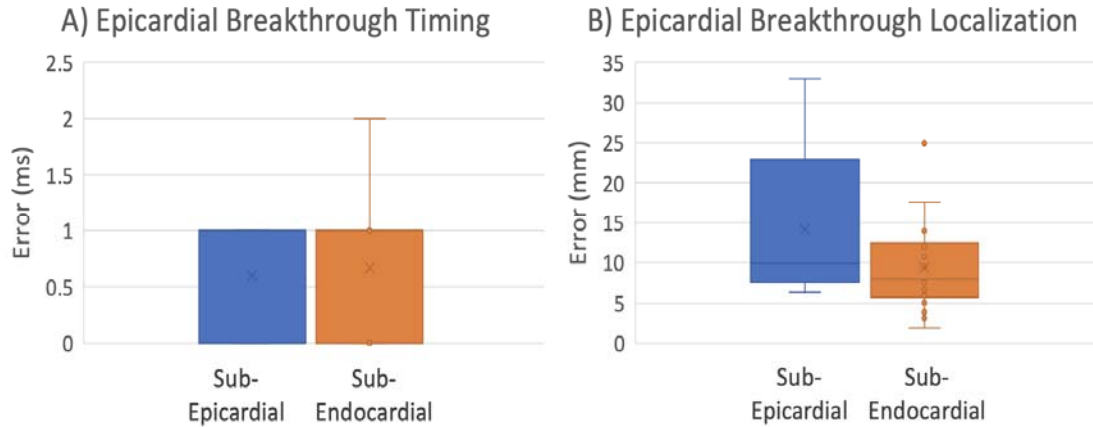
296 In heparinized animals, endocardial mapping of the left ventricle was first performed during
297 sinus rhythm via a retrograde approach using a duodecapolar (20-electrode) catheter
298 (interelectrode spacing = 1-2.5-1 mm, electrode size = 1 mm, AfocusII, St. Jude Medical,
299 Minnetonka, MN) with the NavX mapping system (EnSite Velocity, St. Jude Medical). In
300 addition, a decapolar catheter was advanced from the right jugular vein to the coronary sinus.
301 Programmed ventricular stimulation was performed to induce VT from two right ventricular
302 sites (outflow tract and apex), with up to three extrastimuli decremented to ventricular
303 refractoriness or 250 ms at two drive trains (600 and 400 ms). If VT is induced, mapping
304 during VT was attempted.

305

306 **Results**

307 ***Results on Simulated 3D Reentrant Circuits***

308 The following information were extracted from each reentrant circuit, both simulated “ground
309 truth” and epi-endocardial ECGI solutions: 1) the 3D categorization of reentrant circuits
310 based on qualitative isochrone analysis, 2) the time of epicardial and endocardial
311 breakthrough, and 2) the location of epicardial and endocardial breakthrough (when possible).
312 On the simulated “ground truth” of the reentrant circuit, the central isthmus (if observable)



313 and exits were also identified in 3D to differentiate sub-epicardial, sub-endocardial, and mid-
314 wall circuit exits.

315

316 Below, we first describe the general behavior of ECGI solutions in reconstructing the VT

317 morphology at the epicardial and endocardial surfaces. We then delve into examining the

318 extent to which quantitative metrics – especially the time and location of the surface

319 breakthrough sites – may be extracted from these surface reconstructions to inform 3D

320 location of the reentrant circuits, both in simulated *ground truth* and in ECGI reconstructions.

321

322 Epicardial ECGI solutions: Across all 23 cases, on the epicardium, ECGI was able to

323 reconstruct the electrograms with a reasonable accuracy of spatial correlation coefficients of

324 0.89 ± 0.03 , temporal correlation coefficients of 0.90 ± 0.02 , and a relative mean squared

325 errors (RMSE) of

In all 23 cases, a clear site of the earliest activation could be

326 observed at the epicardium, and was selected as the site of epicardial breakthrough. This

327 resulted in a good accuracy in localizing epicardial breakthrough sites, with 14.17 ± 10.78

328 mm Euclidean distance error in spatial location and 0.6 ± 0.55 ms error in timing for sub-

329 epicardial cases, and 9.39 ± 5.67 mm in spatial location and 0.66 ± 0.59 ms in timing for sub-

Figure 4: Timing (A) and Localization (B) error of Epicardial-breakthrough categorized by sub-epicardial and sub-endocardial groups.

330 endocardial cases, as summarized in Fig. 4. This suggests that the quality of ECGI epicardial
331 solutions was little effected by the intramural location of a reentrant circuit. Diving deeper
332 into the reconstructed epicardial solutions, we noted several limitations. First, when complete
333 circuit including the protected activity within the critical isthmus can be observed in the
334 simulated epicardial data, ECGI reconstruction typically missed such local protected
335 activation shown Fig. 5A. Second, in a small number of cases, ECGI artificially “closed the
336 loop” of the reentrant circuit when the simulated circuit was only partially observed on the
337 epicardium, as illustrated in Fig. 5B. Finally, even as ECGI closely captured the epicardial
338 breakthrough sites, these sites may be far away from the actual exit if the intramural circuits
339 are further beneath the epicardium, as illustrated in Fig. 5C. As a result of these traits,
340 epicardial ECGI alone – despite good performance in capturing gross activation patterns and
341 localizing the site of breakthrough – may have limited ability to inform the 3D construct of
342 the reentrant circuit and its critical isthmus beneath the surface.

343

344 Endocardial ECGI solutions: Across the 23 cases, ECGI solutions on the endocardium was in
345 general poorer in reconstructing the gross activation patterns compared to its epicardial

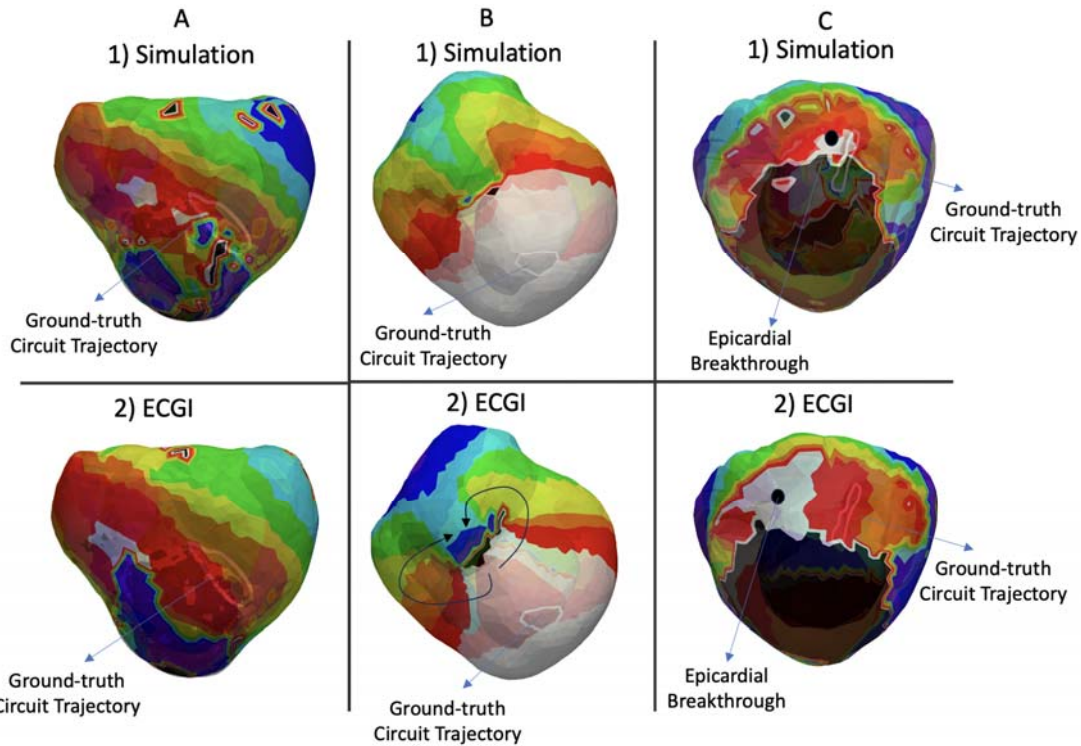


Figure 5: (A) Missing isthmus in ECGI (B) Artificially closing the loop (C) Epicardial breakthrough far from the circuit's exit site.

346 counterpart, with a spatial correlation coefficient of 0.30 ± 0.11 , temporal correlation
347 coefficients of 0.46 ± 0.14 , and a relative mean squared errors (RMSE) of . In all
348 cases, there was no evident site of the earliest activation on the endocardium. Instead, an
349 artificial macroscopic rotation pattern was consistently created in all cases, as illustrated in
350 both example A and example B in Fig. 6.

351

352 Despite the dismal picture the above observations may suggest for endocardial ECGI
353 solutions, accurate timing for detecting endocardial breakthroughs was obtained with LE-
354 based embedding of the temporal trajectory of endocardial activations as described earlier:
355 over the 23 cases, the error in timing endocardial breakthroughs = 0.66 ± 0.59 for sub-
356 endocardial cases and 0.6 ± 0.55 for sub-epicardial cases. In terms of locating the endocardial
357

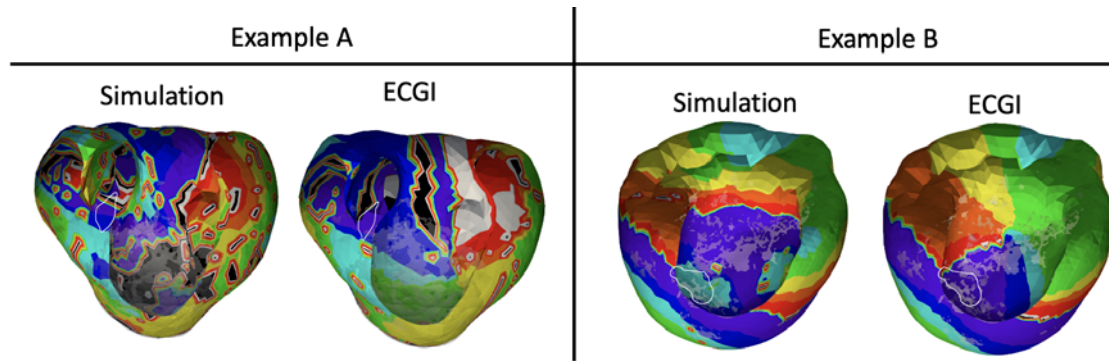


Figure 6: Illustration of the artificial macroscopic rotation pattern created on the endocardial surface by ECGI solutions.

358 breakthrough sites, no clear signature was discovered in the majority of the cases. Below, we
359 examine the utility of these endocardial breakthrough measures – despite the overall low
360 fidelity of activation patterns – in informing the 3D construct of reentrant circuits when
361 combined with epicardial measures.

362

363 3D Categorization of Reentrant Circuits: Fig. 7A summarizes the 3D categorization of the 23
364 simulated reentrant circuits. Out of the 23 circuits, 2D circuits were observed in 26% of the
365 cases (n=6) on the endocardium, whereas 3D circuits were found in 74% of the cases (n=17).
366 23% (n=4) of these 3D circuits were partially observed on only one surface, and one of the
367 circuits was mid-myocardial. None of the reentrant circuits was 3D transmurally uniform.
368 In ECGI reconstruction of these reentrant circuits as summarized in Fig. 7B, 22% were 2D
369 endocardial (n=5), and the rest (78%) were categorized as 3D circuits (n=18). 33% of the 3D
370 circuits were partially observed on only one surface (n=6), and two circuits were
371 reconstructed to be mid-myocardial. None of the ECGI-reconstructed reentrant circuits
372 was 3D transmurally uniform either.

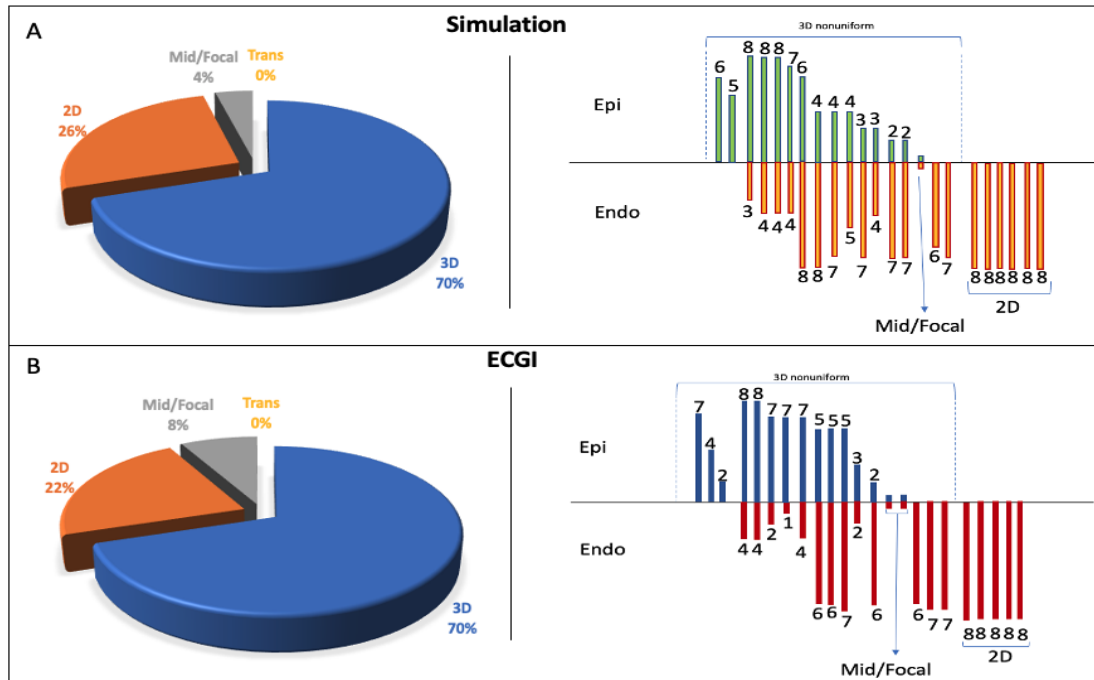


Figure 7: Inferring the 3D category of reentrant circuits using epi-endocardial activation patterns.

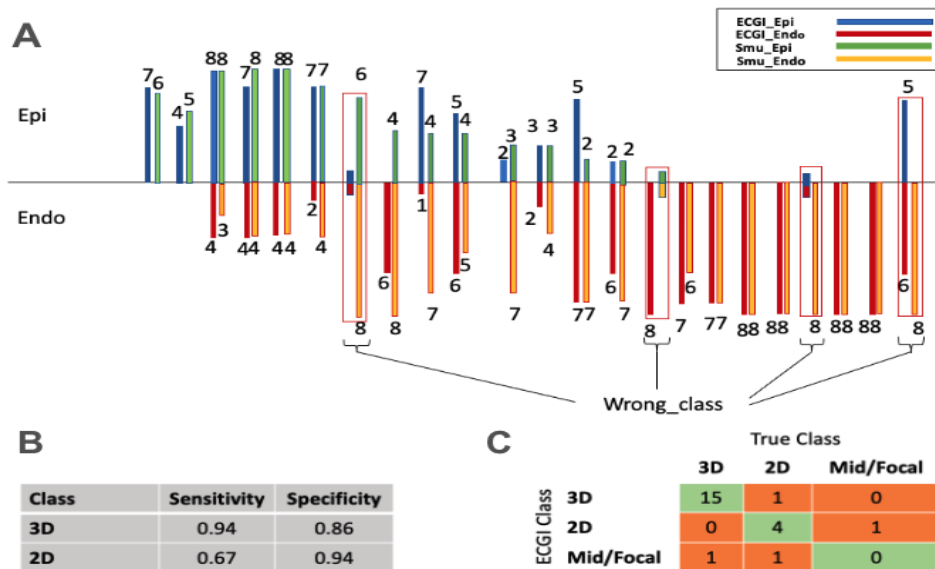


Figure 8: Case-by-case comparison of ECGI recognition of 3D category of reentrant circuits versus simulated ground truth.

373 Fig. 8A details case-by-case evaluations of ECGI's ability to recognize the 3D
374 categorization of reentrant circuits against the simulated ground truth. As shown, ECGI
375 reconstruction correctly preserved the 3D categorization of the reentrant circuits in 82% of
376 the cases (n=19). Out of six 2D reentrant circuits, four (66%) were correctly reconstructed
377 by ECGI. Out of the 17 3D reentrant circuits, 15 (88%) were correctly reconstructed by
378 ECGI. In the four incorrectly reconstructed cases, one mid-myocardial circuit was
379 reconstructed to be 2D endocardial, one endocardial circuit was reconstructed to be mid-
380 myocardial and one reconstructed to be 3D nonuniform, and one 3D non-uniform circuit
381 was reconstructed to be mid-myocardial. Fig. 8B-C summarizes the sensitivity, specificity,
382 and confusion matrix of ECGI in reconstructing 2D and 3D non-uniform cases (mid-
383 myocardial and 3D uniform cases were excluded out of the calculation because of the small
384 number or absence of examples).

385

386 Differentiating sub-endocardial vs. sub-epicardial exits by the timing of epicardial and
387 endocardial breakthroughs: Fig. 9 summarizes the quantitative results of using the delay
388 between epicardial and endocardial breakthroughs in all circuits to differentiate the seven
389 sub-epicardial and 16 sub-endocardial exits, where the latter could be either left or right
390 endocardium as summarized earlier. In simulated data, all reentrant circuits with
391 subendocardial exits were all associated with an epicardial breakthrough lagging the
392 endocardial breakthrough; circuits with sub-epicardial exits were all associated with an
393 epicardial breakthrough preceding the endocardial breakthrough. This was consistently
394 preserved by ECGI in all cases in terms of the sign of the epi-endocardial breakthrough
395 timing delay, as show in Fig. 9 with an absolute error of 1.65 ± 1.46 . This provides initial
396 evidence that the relative order of epi-endocardial breakthroughs in ECGI solutions can

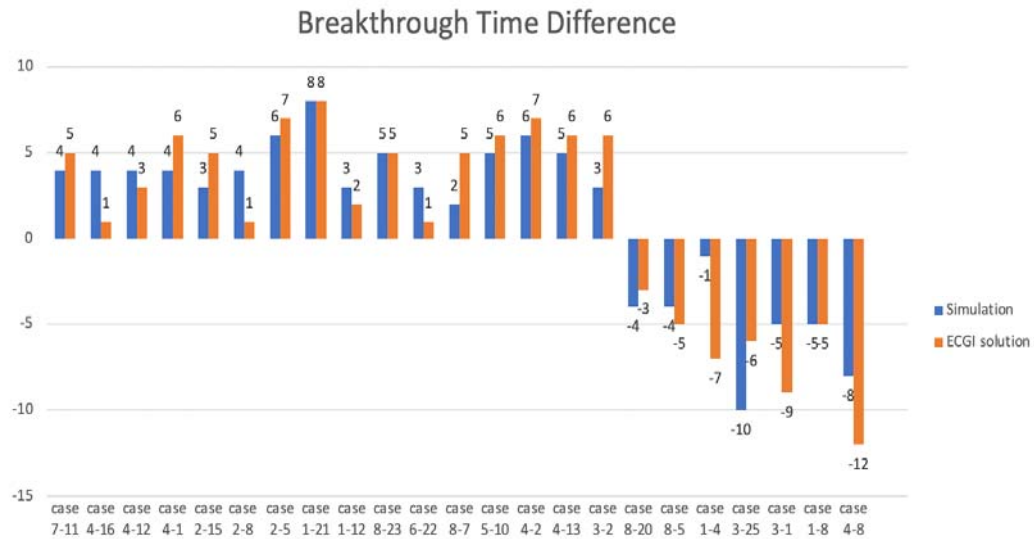


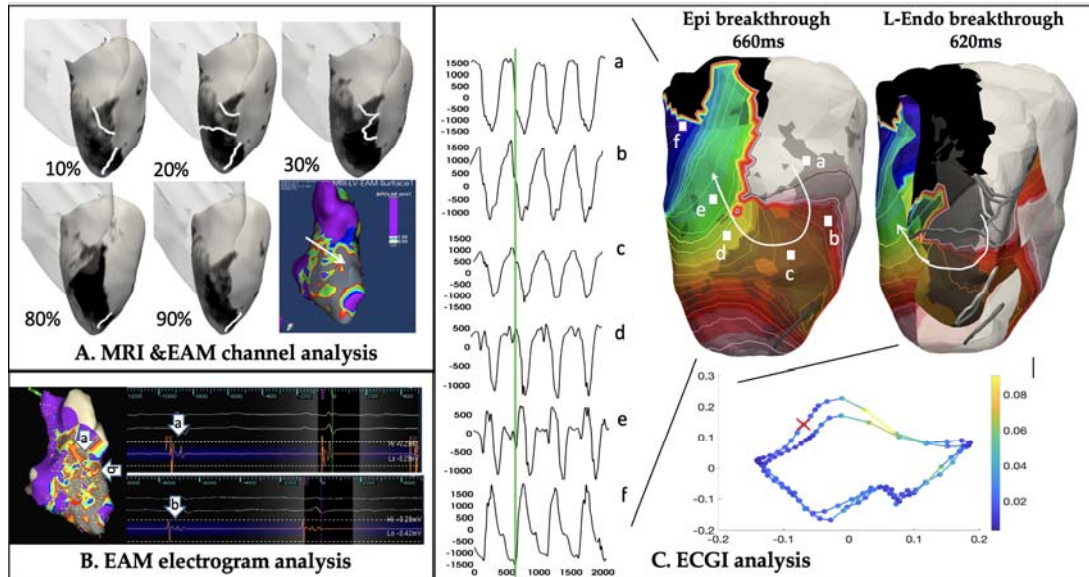
Figure 9: using the delay between epicardial and endocardial breakthroughs to identify the closer surface to the exit site.

397 consistently be used to differentiate whether the circuit exit was closer to the epicardial or
 398 endocardial surfaces.

399

400 ***Results on Chronic Post-Infarction Animal Models of Reentrant Circuits.***

401 A total of four reentrant VT circuits induced in four animal models were studied. From the
 402 DCE-MRI images, ADAS-VT software (ADAS 3D, Galgo Medical, Barcelona, Spain) was
 403 used to delineate possible slow-conducting channels within the myocardial scar. In the
 404 meantime, *in-vivo* EAMs were analyzed to identify local abnormal EGMs such as double
 405 potential, delayed potential, and fractionated potential obtained during sinus rhythm, and
 406 mid-diastolic potential or activation maps obtained during induced VT. These two sources of
 407 data combined provided reference data of the locations of potential critical isthmus for each
 408 of the induced VT circuits. As summarized through Figs 10-13, despite the limited number of
 409 cases, a variety of intramural distributions spanning from sub-endocardial, mid-wall, to sub-



410 epicardial isthmus were observed among the four reentrant circuits. The analyses of ECGI

411 results and MRI/EAM data are carried out by independent operators.

412 Case 1 – sub-endocardial anterior septal circuits: In case 1, DCE-MRI identified conducting

413 channels primarily identified at 10-30% layer of the LV septum at the anterior-septal region,

Figure 10: MRI, EAM and ECGI analysis of animal data, case1 with a sub-endocardial anterior septal circuit.

414 corroborated by the higher-voltage channels detected within the low-voltage area in native-
415 rhythm voltage mapping (Fig 10.A). Fractionated potential was further detected at septal mid-
416 basal-anterior wall during native rhythm electroanatomical mapping (Fig 10.B). In ECGI
417 solutions, the epicardial activation map suggested a breakthrough at mid anterior-septal
418 region of the LV followed by a local clockwise rotation of activation as illustrated by the
419 activation map and selected electrocardiograms (Fig 10.C). ECGI endocardial breakthrough
420 was identified by LE at 40 ms prior to the epicardial breakthrough, followed by

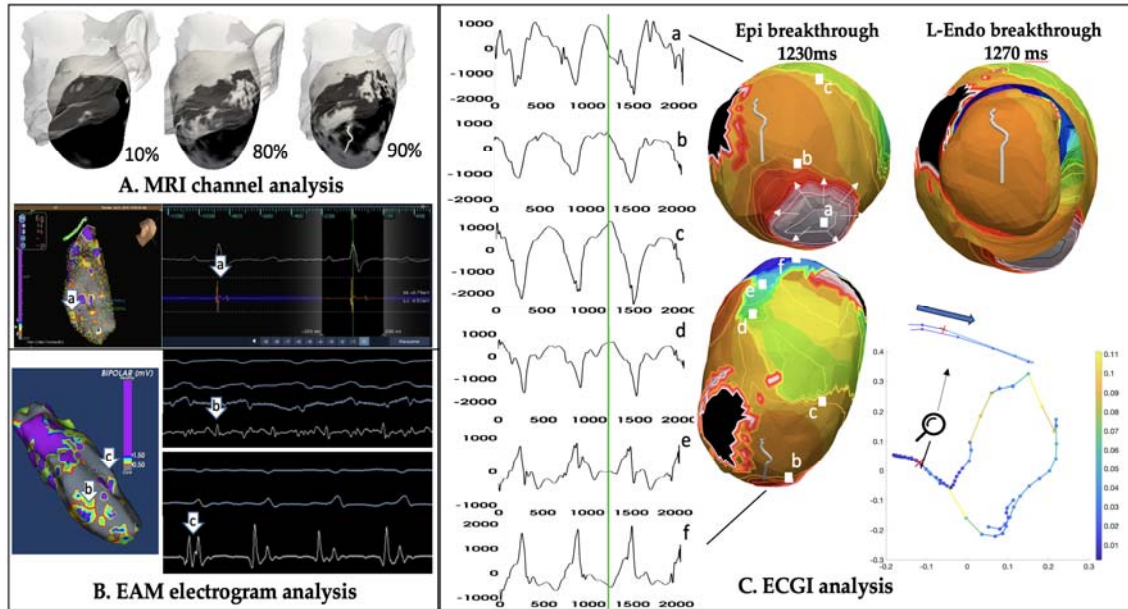


Figure 11: MRI, EAM and ECGI analysis of animal data, case2 with a sub-epicardial apical circuit.

421 also a clockwise rotation with a spatially meandering anchor around the same area on the
422 endocardium (Fig 10.C). This epi-endocardial breakthrough delay suggested a sub-
423 endocardial circuit exit located at mid-basal anterior-septal region of the LV, consistent with
424 the potential channels revealed by combined MRI-EAM analysis.

425 Case 2 – sub-epicardial apical circuits: In case 2, DCE-MRI suggested dense
426 subendocardial scar and potential channels were only detected at 80-90% sub-epicardial layer
427 of the LV (Fig. 11.A). On the EAM, delayed potential was detected around apical septum
428 during native-rhythm mapping, while mid-diastolic and early-systolic potential were detected
429 around apical septum during VT (Fig. 11.B). In ECGI solutions, epicardial activation
430 suggested a breakthrough at the apical region of the LV septum followed by a focal apex-to-
431 base activation as illustrated by the activation map and selected electrocardiograms (Fig.

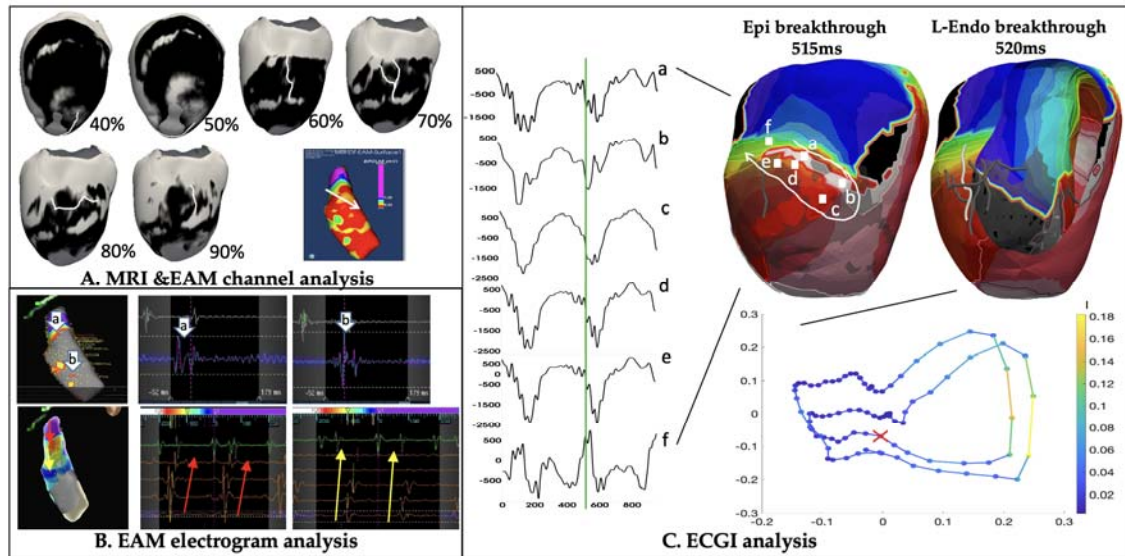
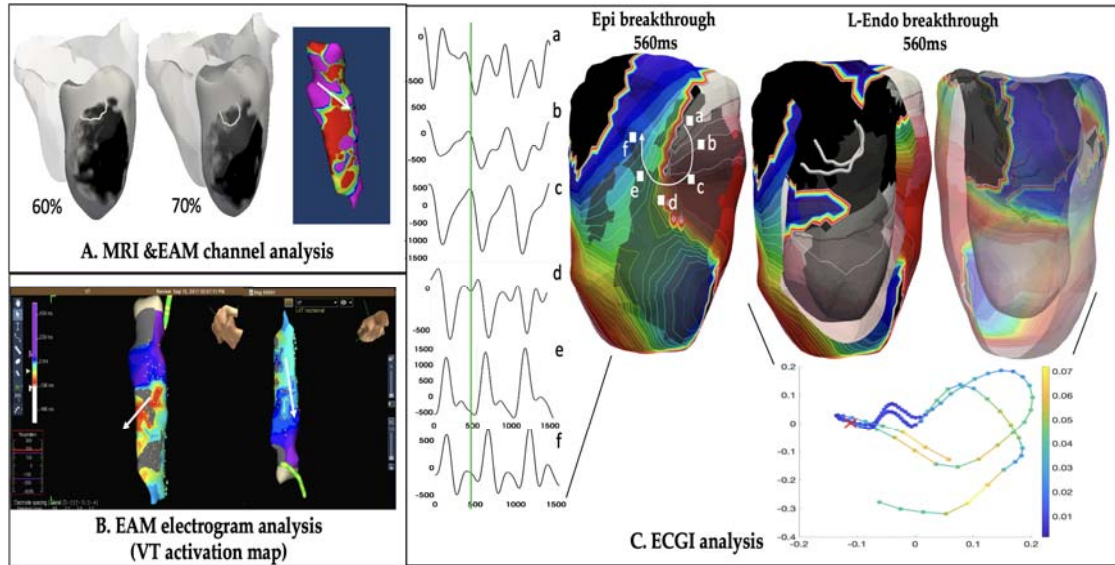


Figure 12: MRI, EAM and ECGI analysis of animal data, case3 with a mid-wall mid-basal anterior-septal circuit.

432 12C). ECGI endocardial breakthrough was identified by the LE at 40-50 ms after the
433 epicardial breakthrough, with a counterclockwise rotation anchored on the mid-septum of the
434 LV endocardium (Fig. 11C). This epi-endocardial breakthrough delay suggested a sub-
435 epicardial critical channel, located at apical septum of the LV. This was consistent with one
436 of the only two DCE-MRI derived channels at 90% layer (*i.e.*, sub-epicardial layer) of the LV
437 septum and the EAM data.

438 Case 3-4: – Mid-wall mid-septum and anterior circuits: In case 3, DCE-MRI suggested
439 apical channels at the mid-layer (40-50%) of the LV, and mid-basal lateral-anterior region
440 (60-90%) of the LV septum – the latter consistent with higher-potential channel revealed
441 within the low-voltage region during native-rhythm voltage mapping (Fig 12 A). Additionally,
442 double potential was detected at basal and mid-anterior LV during native-rhythm mapping,
443 while mid-diastolic potential around the same region was detected during VT (Fig 12 B). In
444 ECGI solutions, epicardial solutions suggested a breakthrough at mid-basal anterior-septal



445 region of the LV followed by a local clockwise rotation, as illustrated by the activation map
446 and selected electrocardiograms (Fig 12 C). ECGI endocardial breakthrough was identified at
447 5 ms after epicardial breakthrough, with a counter-clockwise rotation with a meandering
448 anchor in mid-to-apical septal region of the LV endocardium. This epi endocardial
449 breakthrough delay suggested a mid-wall to sub-epicardial circuit exit located at

Figure 13: MRI, EAM and ECGI analysis of animal data, case4 with a mid-wall circuit located at basal lateral-anterior region of the LV septum.

450 mid-basal anterior-septal region of the LV, consistent with a series of potential channels

451 identified at 60-90% layer channels identified by combined MRI-EAM analysis.

452

453 In case 4, DCE-MRI again suggested relative dense scar with basal lateral-anterior channels,

454 corroborated by the relatively higher-voltage channel identified within the low voltage area

455 during native-rhythm voltage mapping (Fig. 13A). VT activation map obtained by EAM

456 suggested an early activation at mid-anterior region of the LV septum and an apex-to-base

457 activation pattern at the inferior region of the LV (Fig. 13B). In ECGI solutions, epicardial

458 activation showed a breakthrough at mid-basal lateral-anterior region of the LV septum,

459 leading to a local clockwise rotation near the mid-basal anterior-septal region as illustrated by

460 the activation map and selected electrocardiograms (Fig. 13C). ECGI endocardial

461 breakthrough was identified by the LE almost simultaneously with the epicardial

462 breakthrough, with a clockwise rotation and a meandering anchor at a similar location to that

463 on the epicardium. This epi-endocardial breakthrough delay suggested a mid-wall critical

464 channel located at basal lateral-anterior region of the LV septum, consistent with the

465 combined MRI-EAM analysis. Furthermore, note that in this case, the endocardial activation

466 map also showed an early activation at mid-anterior region of the LV septum and an apex-to-

467 base rotation on the inferior region, as that mapped during VT *in-vivo*.

468

469 Overall, across the four reentrant circuits, it was observed that epicardial ECGI solutions

470 revealed breakthrough sites and general rotation patterns qualitatively consistent with the

471 general location of MRI-EAM suggested sites of critical isthmuses. Details on the activation
472 maps, however, were not sufficient to reveal further information about the potential entrance
473 sites of the local reentrant circuits nor the exact pinpointing of the exit sites, potentially
474 because the signals of the local reentrant circuit was dominated by the global activation
475 pattern throughout the ventricles. Validity on the activation pattern of ECGI endocardial
476 solutions or breakthrough sites was less conclusive. Despite these limitations, the relative
477 timing of epi-endocardial ECGI breakthroughs consistently revealed the proximity of the
478 potential circuit exits to the epicardial or endocardial surfaces, as supported by the combined
479 MRI-EAM analyses – suggesting a potential clinical value for epi-endocardial ECGI in
480 informing ablation strategies.

481

482 **Conclusions**

483 While the use of simulation data warrants further translations to experimental or clinical data,
484 it enabled mechanistic investigations of the relation between detailed 3D morphology of
485 reentrant circuits and their observations on epi-endo surfaces. The extension to *in-vivo* animal
486 model and human subject data further provided a proof of concept that simultaneous epi-endo
487 mapping, especially the timing and location of epi-endocardial breakthrough sites, may
488 provide important information for inferring the 3D morphology of the reentrant circuits.
489 ECGI, as a noninvasive technique for rapid and simultaneous epi-endo mapping, may play an
490 important role in revealing the hidden components of a 3D reentrant circuits that is currently
491 not possible. This has potential to enable further 3D mechanistic studies of VT morphologies
492 or guiding ablation strategies in a way that is not possible with current practice.

493 **Funding Sources**

494 This study was supported by grants from the National Institutes of Health under grant number
495 R15HL140500, the National Science Foundation under grant number ACI-1350374, and the
496 Cardiac Arrhythmia Network of Canada.

497 **References**

- 498 1. Chillou C de, Lacroix D, Klug D, Magnin-Poull I, Marquie C, Messier M, et al. Isthmus
499 characteristics of reentrant ventricular tachycardia after myocardial infarction.
500 *Circulation*. 2002;105:726–31.
- 501 2. Wissner E, Stevenson WG, Kuck KH. Catheter ablation of ventricular tachycardia in
502 ischaemic and non-ischaemic cardiomyopathy: where are we today? A clinical review.
503 *Eur Heart J*. 2012 Jun;33(12):1440–50.
- 504 3. Tung R, Raiman M, Liao H, Zhan X, Chung FP, Nagel R, et al.
505 Simultaneous endocardial and epicardial delineation of 3d reentrant ventricular
506 tachycardia. *J Am Coll Cardiol*. 2020;75(8):884–97.
- 507 4. Stevenson WG. Current treatment of ventricular arrhythmias: state of the art. *Heart*
508 *Rhythm Off J Heart Rhythm Soc*. 2013 Dec;10(12):1919–26.
- 509 5. Haissaguerre M, Hocini M, Shah AJ, Derval N, Sacher F, Jais P, et al. Noninvasive
510 Panoramic Mapping of Human Atrial Fibrillation Mechanisms: A Feasibility Report. *J*
511 *Cardiovasc Electrophysiol*. 2013;24(6):711–7.
- 512 6. van Dam PM, Tung R, Shivkumar K, Laks M. Quantitative localization of premature
513 ventricular contractions using myocardial activation ECGI from the standard 12-lead
514 electrocardiogram. *J Electrocardiol*. 2013 Dec;46(6):574–9.

- 515 7. Burnes JE, Taccardi B, Rudy Y. A Noninvasive Imaging Modality for Cardiac
516 Arrhythmias. *Circulation*. 2000;102(21):2152–8.
- 517 8. Burnes JE, Taccardi B, Ershler P, Rudy Y. Noninvasive Electrocardiogram Imaging of
518 Substrate and Intramural Ventricular Tachycardia in Infarcted Hearts. *J Am Coll Cardiol*.
519 2001;38(7):2071–8.
- 520 9. Cuculich PS, Schill MR, Kashani R, Mutic S, Lang A, Cooper D, et al. Noninvasive
521 Cardiac Radiation for Ablation of Ventricular Tachycardia. *N Engl J Med*.
522 2017;377:2325–36.
- 523 10. Sapp JL, Dawoud F, Clements JC, Horáček BM. Inverse Solution Mapping of
524 Epicardial Potentials: Quantitative Comparison with Epicardial Contact Mapping. *Circ*
525 *Arrhythm Electrophysiol*. 2012;5(5):1001–9.
- 526 11. Wang Y, Cuculich PS, Zhang J, Desouza KA, Vijayakumar R, Chen J, et al.
527 Noninvasive Electroanatomic Mapping of Human Ventricular Arrhythmias with
528 Electrocardiographic Imaging. *Sci Transl Med*. 2011;3(98):98ra84.
- 529 12. Robinson CG, Samson PP, Moore KMS, Hugo GD, Knutson N, Mutic S, et al. Phase
530 I/II Trial of Electrophysiology-Guided Noninvasive Cardiac Radioablation for
531 Ventricular Tachycardia. *Circulation*. 2019;139:313–21.
- 532 13. Graham AJ, Orini M, Zacur E, Dhillon G, Daw H, Srinivasan NT, et al. Evaluation of
533 ECG Imaging to Map Hemodynamically Stable and Unstable Ventricular Arrhythmias.
534 *Circ Arrhythm Electrophysiol*. 2020;13:e007377.

- 535 14. Tsyganov A, Wissner E, Metzner A, Mironovich S, Chaykovskaya M, Kalinin V, et al.
536 Mapping of ventricular arrhythmias using a novel noninvasive epicardial and
537 endocardial electrophysiology system. *J Electrocardiol*. 2018;51(1):92–8.
- 538 15. Wang L, Gharbia OA, Nazarian S, Horacek BM, Sapp JL. Non-invasive epicardial and
539 endocardial electrocardiographic imaging for scar-related ventricular tachycardia.
540 *Europace*. 2018;20:f263–72.
- 541 16. Pashakhanloo F, Herzka D, Halperin H, McVeigh E, Trayanova N. Role of 3-
542 Dimensional Architecture of Scar and Surviving Tissue in Ventricular Tachycardia
543 Insights From High-Resolution Ex Vivo Porcine Models © 2018 American Heart
544 Association, Inc. Farhad. *Circ Arrhythm Electrophysiol*. 2018;11:e006131.
- 545 17. Plonsey R. *Bioelectric Phenomena*. New York: McGraw Hill; 1969.
- 546 18. Gockenbach M. *Linear Inverse Problems and Tikhonov Regularization*. Mathematical
547 Association of American; 2016. (Carus Mathematical Monographs).
- 548 19. Burton BM, Tate JD, Erem B, Swenson DJ, Wang DF, Steffen M, et al. A Toolkit for
549 Forward/Inverse Problems in Electrocardiography Within the SCIRun Problem Solving
550 Environment. In: *IEEE Eng Med Biol Soc*. 2011. p. 267–70.
- 551 20. Umopathy K, Nair K, Masse S, Krishnan S, Rogers J, Nash MP, et al. Phase Mapping of
552 Cardiac Fibrillation. *Circ Arrhythm Electrophysiol*. 2010;3(1):105–14.
- 553 21. Vijayakumar R, Vasireddi SK, Cuculich PS, Faddis MN, Rudy Y. Methodology
554 Considerations in Phase Mapping of Human Cardiac Arrhythmias. *Circ Arrhythm
555 Electrophysiol*. 2016;9(11):e004409.

- 556 22. Arevalo H, Vadakkumpadan F, Guallar E, Jebb A, Malamas P, Wu KC, et al.
557 Arrhythmia risk stratification of patients after myocardial infarction using personalized
558 heart models. *Nat Commun.* 2016;7:11437.
- 559 23. Wang L, Zhang H, Wong K, Liu H, Shi P. Physiological-Model-Constrained
560 Noninvasive Reconstruction of Volumetric Myocardial Transmembrane Potentials.
561 *IEEE Trans Biomed Eng.* 2010;57(2):296–315.
- 562 24. Pashakhanloo F, Herzka D, Mori S, Zviman M, Halperin H, Gai N, et al. Submillimeter
563 diffusion tensor imaging and late gadolinium enhancement cardiovascular magnetic
564 resonance of chronic myocardial infarction. *J Cardiovasc Magn Reson Off J Soc*
565 *Cardiovasc Magn Reson.* 2017;1–14.
- 566 25. C. L. Hubley-Kozey, L. B. Mitchell, Gardner MJ, Warren JW, Penney CJ, Smith ER, et
567 al. Spatial features in body-surface potential maps can identify patients with a history of
568 sustained ventricular tachycardia. *Circulation.* 1995;92:1825–38.
- 569 26. Belkin M, Niyogi P. Laplacian eigenmaps for dimensionality reduction and data
570 representation. *Neural computation.* 2003 Jun 1;15(6):1373-96.
571